Climate Dynamics (2023) 61:3935–3953
https://doi.org/10.1007/s00382-023-06779-7

Dynamic and thermodynamic processes related to precipitation diurnal cycle simulated by GRIST

Yihui Zhou[1] · Rucong Yu[1] · Yi Zhang[2,3] · Jian Li[1]

Received: 24 November 2022 / Accepted: 4 April 2023 / Published online: 15 April 2023

Abstract
Most state-of-the-art general circulation models cannot well simulate the diurnal cycle of precipitation, especially the nocturnal rainfall peak over land. This study assesses the diurnal cycle of precipitation simulated using the Global-to-Regional Integrated forecast SysTem (GRIST) in its numerical weather prediction (NWP) configuration at resolutions typical of current global climate models. In the refinement region, the variable-resolution model well distinguishes the distinct features of diurnal cycle. No apparent artificial features are observed in the transition zone of the variable-resolution mesh. The model also exhibits a similar diurnal cycle pattern to the observation in the coarse-resolution region. We further investigate the model behaviors of dynamics–physics interaction by analyzing hourly dynamical and thermodynamical diagnostics. Composite analysis based on rainfall peak time is applied to examine the model capability in distinguishing different precipitation processes of daytime and nighttime peaks. Over East Asia, the model well reproduces both the nocturnal-to-early-morning and the afternoon rainfall peaks. The model simulates the dominant contribution of large-scale upward moisture advection to the formation of stratiform-like rainfall peaks, and produces daytime surface-heating induced rainfall. Refinement of the resolution substantially increases the composited nighttime precipitation intensity but has little impact on the composite percentage. The model captures the realistic dynamical and thermodynamical conditions for the occurrence of nocturnal rainfall. These results demonstrate that the variable-resolution model is able to reproduce the diurnal cycle of climatological summer rainfall through realistic precipitation processes.

Keywords Precipitation diurnal cycle · Dynamic and thermodynamic processes · Variable-resolution model · Nocturnal rainfall

1 Introduction

The diurnal cycle is a basic mode for assessment of the model behavior, particularly with regard to understanding interactions between model dynamics and physics. Simulating the diurnal cycle of global precipitation patterns remains difficult for current global models (Christopoulos and Schneider 2021; Lee and Wang 2021; Watters et al. 2021). Typical model biases include early occurrence of the continental rainfall maxima, absence of nocturnal rainfall peaks, and deficiency in propagating rainfall signals across grid points (e.g., Bechtold et al. 2004; Yu et al. 2014; Covey et al. 2016; Xie et al. 2019). These problems are generally ascribed to the inability of the moist physical processes to respond to various large-scale controls and surface heating patterns.

Previous related studies indicated that simulating the diurnal cycle of precipitation is a highly model-dependent issue. Higher-resolution models do not necessarily produce better performance than lower-resolution models (Dirmeyer et al. 2012; Yuan 2013), unless certain key physical processes can be properly represented by the physics-dynamics interaction. For example, increasing the horizontal resolution of a super-parameterization global model improves the simulated diurnal cycle, while such beneficial resolution

✉ Rucong Yu
yrc@cma.gov.cn

✉ Yi Zhang
zhangyi_fz@piesat.cn

[1] State Key Laboratory of Severe Weather (LASW), Chinese Academy of Meteorological Sciences, Beijing, China

[2] 2035 Future Laboratory, PIESAT Information Technology Co., Ltd., Beijing, China

[3] Beijing Research Institute, Nanjing University of Information Science and Technology, Beijing, China

sensitivity is not supported by a conventional-parameterization model (Zhang and Chen 2016; Zhang et al. 2019a). For a fixed model, increasing the resolution alone generally improves simulation performance to various extents, but seems not to fundamentally alter certain intrinsic model deficiencies (Kim et al. 2019; Love et al. 2011; Hohenegger et al. 2020). Meanwhile, the typical understanding that convection-permitting modeling improves simulated diurnal cycles (e.g., Yun et al. 2020; Li et al. 2021) is based not only on the effect contributed by the resolution itself, but also on the different approach to simulation of moist physical processes. Certain advantages of the models configured with a "convection-permitting" setup can also be found in their lower-resolution simulations (e.g., Sato et al. 2009; Yashiro et al. 2016; Zhang et al. 2022).

The Global-to-Regional Integrated forecast SysTem (GRIST) was developed with the objective of unified weather and climate modeling by coupling different weather and climate physics suites to a common dynamical core framework (Wang et al. 2019; Zhang et al. 2019b, 2020, 2021, 2022; Zhou et al. 2020; Liu et al. 2020; Li and Zhang 2022; Li et al. 2022). Previous work established a baseline model formulation targeting unified weather-to-climate forecast applications (Zhang et al. 2021). Here, this model is referred to as GRIST-NWP, because its physics suite (see Sect. 2.1) inherits some design choices typically used for high-resolution mesoscale weather forecast applications, and to distinguish it from another "typical climate model" setup of GRIST that uses a physics package originally designed for long-term climate simulation (Li et al. 2022, 2023). GRIST-NWP has been used increasingly in certain experimental and operational weather-to-climate forecast applications, including global storm-resolving simulations as part of the DYnamics of the Atmospheric general circulation Modeled On Non-hydrostatic Domains (DYAMOND) winter project. Its global 0.125° quasi-operational NWP setup is also currently under development and is tested at PIESAT Information Technology Co., Ltd. (Wang et al. 2022).

For a fixed model system, performing lower-resolution climate simulations can help in assessment of the systematic behaviors of high-resolution weather models (e.g., Fang et al. 2017; Roberts et al. 2018), which can expose the model errors related to certain leading-order features such as large-scale circulations and associated rainfall patterns. Meanwhile, GRIST supports global variable-resolution (VR) simulations (Zhou et al. 2020). Previous studies have examined the impact of regional modeling using the VR approach. While the specific refinement approaches might differ, these VR models generally benefit from finer grid spacing (e.g., Gettelman et al. 2018; Zhao et al. 2019; Zhou et al. 2020). Simulations over a refinement region can be comparable with (quasi) uniform high-resolution simulations. Typically, VR models are able to capture fine-scale atmospheric processes, such as tropical cyclones (Zarzycki and Jablonowski 2014; Michaelis and Lackmann 2019) and mesoscale convective systems (Feng et al. 2021), and provide solution quality competitive with that of traditional limited-area climate modeling (Huang et al. 2016; Rahimi et al. 2019). Upscaling effects from the refinement regions on the large-scale circulation or key systems outside the refined domain can also be observed (Hashimoto et al. 2016).

Focusing on East Asia, Zhang et al. (2021) analyzed GRIST-simulated precipitation features. Results demonstrated that GRIST could well distinguish both the afternoon and the nocturnal-to-early-morning rainfall peaks over various regions in China, and that the model produced reasonable diabatic heating in response to daytime surface heating and nighttime large-scale dynamical forcing (e.g., moisture convergence). The propagating rainfall episodes from the eastern periphery of the Tibetan Plateau to its lee side were best captured using a VR configuration with the region of highest local resolution over eastern China. This was accompanied by a transitional response of the diabatic heating patterns from an upstream-convective type to a downstream-stratiform type.

Zhang et al. (2021) mainly focused on the climatological mean state, while the detailed dynamical and thermodynamical structures related to different rainfall peaks were not investigated. It is unclear whether the model captures the diurnal cycle features through realistic precipitation processes. Meanwhile, because global models adopt one formulation across all regions, it remains a challenge to simultaneously reproduce different types of precipitation features in different regions. It is not well understood whether the model behaves properly in other regions over the globe. Considering potential differences in the dynamical and thermodynamical conditions, a model might behave well for one region but produce degraded performance for another (Liang 2004). In this study, broader evaluation of global rainfall patterns is performed for boreal summer. Meanwhile, in-depth analysis is conducted on the diurnal cycle of precipitation in East Asia with emphasis on the precipitation processes.

The remainder of this paper is organized as follows. Section 2 describes the model, experiments, reference datasets, and the analysis methods adopted in this study. Section 3 evaluates the simulated diurnal cycle of precipitation. Section 4 investigates the modeled dynamics–physics interaction on the diurnal scale. Finally, a summary is presented in Sect. 5.

2 Model, experiments, and methods

2.1 Model

GRIST is a unified model system for weather and climate modeling. Its dynamical core solver is characterized by a

layer-averaged dry-air-mass unstructured C-grid discretization approach, which supports unified hydrostatic and nonhydrostatic, uniform-resolution and variable-resolution modeling within a single integration flow (Zhang 2018; Zhang et al. 2019b, 2020, 2021; Zhou et al. 2020). Its physics-dynamics coupling allows use of different application-specific physics suites optimally designed for conventional weather and climate modeling applications (Zhang et al. 2020).

A detailed introduction to the physics schemes and the model configurations relevant to this study can be found in Zhang et al. (2021). The major physics schemes include the convective scheme (Bechtold et al. 2008; Zhang and Wang 2017), cloud microphysics (Hong and Lim 2006), radiation transfer (Mlawer et al. 1997; Iacono et al. 2008), cloud fraction (Collins et al. 2004), boundary layer processes (Hong et al. 2006) and a land surface model (Niu et al. 2011; Yang et al. 2011). The convection scheme is a modified Tiedtke scheme applied in the Integrated Forecasting System (Bechtold et al. 2014a) and has been tested for high-resolution regional climate modeling (Zhang and Wang 2017). The modified Tiedtke scheme can largely improve the simulations on tropical variations and the diurnal cycle of precipitation through new trigger functions, convection closures and other modifications (Bechtold et al. 2014b). The microphysics scheme is the WRF single-moment six-class scheme with six prognostic water substance variables. The scheme is explicitly coupled to grid-scale dynamics and moisture and produces grid-scale precipitation.

2.2 Model experiments and reference datasets

The Atmospheric Model Intercomparison Project experiment was initiated on May 26, 2000, and this study used June-July-August (JJA) hourly data (2002–2006) for the analysis. An experiment based on a quasi-uniform 120-km mesh (i.e., QU-120 km) was used as the control experiment. Given the complex multiscale interactions and distinctive topographic features over East Asia, we refined the resolution of this area to ~35 km (VR-EA; Fig. 1) to examine the VR performance. The transition zone covered the Indian monsoon region, which is a proper testing scenario for identifying certain potential problems (e.g., numerical artifacts) associated with VR simulations. The resolution of the coarse region was ~110 km, i.e., close to that of the control experiment.

The reference data included the following observational and reanalysis datasets. (1) Integrated Multisatellite Retrievals for Global Precipitation Measurement (IMERG) precipitation data (Huffman et al. 2019) from 2002 to 2006. This 30-min dataset has been converted to the hourly time scale. (2) Hourly gauge-satellite merged precipitation data covering an area within 15° –60° N and 70°–140° E (CMPA; Shen et al. 2014) from 2008 to 2012. (3) Hourly ERA5 precipitation data (Hersbach et al. 2020) from 2008 to 2012.

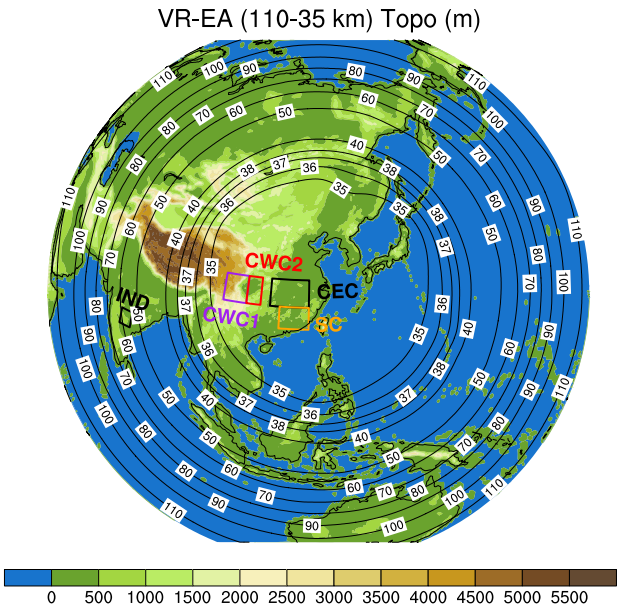

Fig. 1 Variable-resolution mesh with the refinement center in East Asia. Contours denote the mesh resolution (km) and color shading shows surface elevation (m). Boxes delineate most of the selected regions (excluding southeast U.S. in the coarse-resolution region) with typical diurnal precipitation features, including central eastern China (CEC), central western China on the lee side of the Tibetan Plateau with high topography (CWC1) and downstream of the Tibetan Plateau with low topography (CWC2), southern China (SC), and India (IND)

2.3 Analysis methods

The simulated diurnal cycle of precipitation was compared with the observations and reanalysis data. All the reference data and model simulation data were interpolated to a 1° × 1° grid by performing a distance-weighted average remapping of the nearest neighbors' value for analysis (excluding the ERA5 reanalysis data highlighted in Sect. 4.2). First, the 5-year JJA mean diurnal cycle of precipitation was calculated. The peak time of the diurnal cycle is the local standard time (LST) of the maximum precipitation rate. The amplitude of the diurnal cycle was calculated as the ratio of the difference between the maximum and mean precipitation to the mean precipitation.

Given the 5-year JJA mean diurnal cycle precipitation P, harmonic analysis was performed to extract each harmonic component of the diurnal cycle (Dai 2001):

$$P(t) = P_0 + S_1(t) + S_2(t) + \text{residual} \tag{1}$$

$$S_n(t) = A_n \sin\left(n\frac{2\pi}{T}t + \sigma_n\right) \tag{2}$$

where P_0 is the daily mean value, S_n is the n-th harmonic component of the diurnal cycle, A_n is the amplitude of the n-th harmonic component, σ_n is the phase, T is the original period of the time series (i.e., 24 h), and t is the LST. Here, $n = 1$ means the first harmonic component of the diurnal cycle that we analyzed in this study.

To understand the discrepancies in the diurnal cycle of precipitation between the two model simulations, we diagnosed their hourly-scale apparent heat source (Q_1), apparent moisture sink (Q_2), and large-scale vertical advection of water vapor mixing ratio (Yanai et al. 1973; Zhang et al. 2021). With radiation heating (Q_R) removed, $Q_1 - Q_R$ represents the bulk effect of vertical eddy heat transport and heat release/loss due to phase change, while $Q_1 - Q_2 - Q_R$ represents the vertical eddy transport of total heat, reflecting subgrid-scale convective activity (Yanai et al. 1973). The diagnostics analyzed here are model-dependent residual diabatic tendencies that are highly related to the model physics. Unlike atmospheric state variables, the residual diabatic tendencies derived from reanalysis data (e.g., ERA5) would not provide useful comparison with the model because the residual term is computed in a highly nonlinear way and is tightly related to model physics. However, it is useful to compare the residual physical tendencies to investigate the resolution sensitivity within a single model.

Because daytime and nighttime rainfall events are typically caused by different physical mechanisms, we divided an entire day into four phases characterized by the rainfall peak time (i.e., 0000–0600, 0600–1200, 1200–1800, and 1800–2400 LST). The precipitation rates and diagnostics of diabatic heating tendencies were then composited for each phase. Although dividing a day into two phases (e.g., 2000 and 0800 LST) may also be beneficial to separating daytime and nighttime rainfall events, the four phases applied here helps to illustrate more detailed processes. As will be shown in the results, there is difference in the structure of heating pattern and vertical advection of water vapor between certain adjacent phases (e.g., 0000–0600 LST and 0600–1200 LST phase). The model sensitivity to resolution even exhibits larger discrepancies over certain region. The ratio between the number of times when the rainfall peaks fell within a given phase and the total number of days (i.e., 460 days for this study) was calculated to determine the contribution of each phase. In this way, we extracted the specific dynamical and physical interaction for a given precipitation type.

3 Mean states of precipitation

In the IMERG data, the JJA mean precipitation is characterized by a band of heavy rainfall located at the north of the equator (Fig. 2a). The intertropical convergence zone roughly forms the rainfall band with convergence of trade winds. The difference between ERA5 and IMERG is small, and their spatial correlation coefficient is 0.92. The major differences are located around the Maritime Continent, along the band of heavy rainfall, and in the mountainous regions (Fig. 2b). The overall pattern of precipitation bias in QU-120 km is similar to that of ERA5, although differences can be observed over certain regions (Fig. 2c). When the local horizontal resolution is refined to ~35 km over East Asia, the dry biases in southern China and the cold biases in northern China decrease (Fig. 2d). Outside the refinement region, VR-EA generally preserves the distribution of

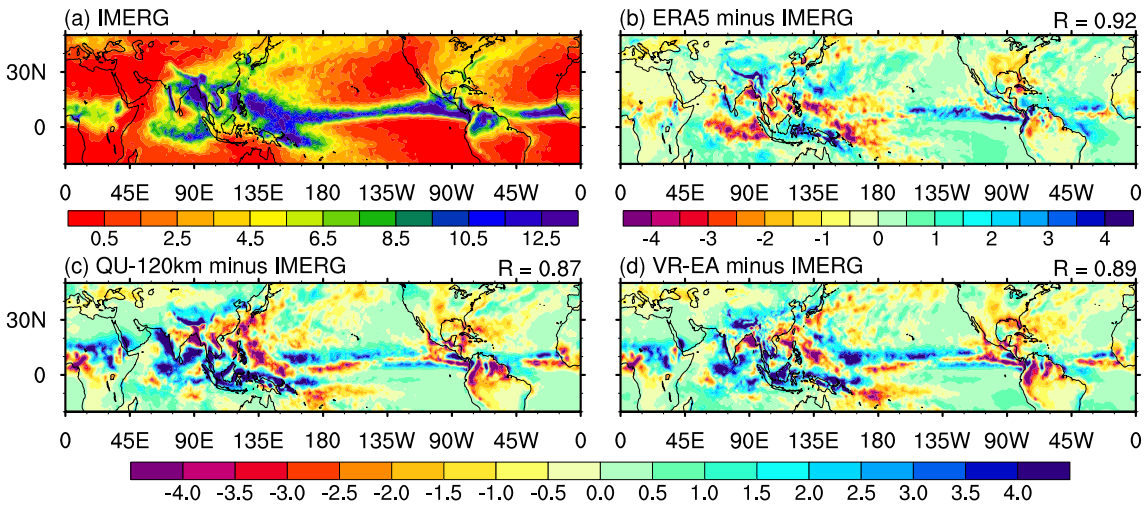

Fig. 2 Climatological mean total precipitation rates (mm/d) between 20° S and 50° N during JJA for **a** IMERG, **b** ERA5 minus IMERG, and GRIST simulations minus IMERG comprising **c** QU-120 km and **d** VR-EA. The spatial correlation coefficient of precipitation between IMERG and the ERA5/model simulations over the globe (within 50° S and 50° N; full available area of the IMERG data) is given to the right zone above each subplot

QU-120 km. Improvements can also be found over certain regions, including alleviation of artificial precipitation over the southern Arabian Peninsula where root mean square error (RMSE) reduces from 5.74 to 4.34, and a more realistic pattern of precipitation over the Indian Ocean and eastern Amazon regions. The spatial correlation coefficient is increased from 0.87 to 0.89. VR-EA also has lower RMSE and higher correlation coefficient over the refinement region, transition zone, and coarse-resolution region, respectively (Table 1).

Figure 3 shows the local time peak and amplitude of the diurnal cycle of total precipitation rates. IMERG shows late-afternoon peaks dominating over the land and nocturnal-to-early-morning peaks dominating over the ocean (Fig. 3a), consistent with previous studies based on different observational products (Watters and Battaglia 2019; Tang et al. 2021). Diverse diurnal features can be found over certain regions with specific topography, e.g., the nocturnal-to-early-morning peaks on the lee side of the Tibetan Plateau. In comparison with IMERG, the precipitation of ERA5 tends to occur earlier over the major continents and partially reflects the nocturnal peaks over North America (Fig. 3b). However, ERA5 barely reproduces the nocturnal-to-early-morning peaks downstream of the Tibetan Plateau nor the nocturnal peaks over the southern slopes of the Tibetan Plateau.

In the coarse-resolution region, the features of rainfall diurnal cycle in VR-EA are reasonably similar to those of QU-120 km (Fig. 3c, d). Over North America, GRIST (QU-120 km and VR-EA) broadly captures the eastward delay in the peak time of precipitation downstream of the Rockies Mountains, although the location of the transition from the afternoon peak to the midnight peak in the model drifts to the east of that presented in IMERG and ERA5. Model deficiency in earlier afternoon peak phase may be generally attributable to the convective scheme, which can be tuned through convective closure and convective time scales. The deficiency in reproducing the nocturnal precipitation peak and the eastward propagation of convective systems downstream of the Rocky Mountain could be improved through modified convective schemes or convection permitting modeling (e.g., Xie et al. 2019; Scaff et al. 2019). In Africa, GRIST overall reproduces the afternoon peak features but with earlier peak time. In addition, discrepancies in the distribution of nighttime rainfall peak between the model and IMERG can also be identified. In South America, GRIST reproduces a more realistic pattern of the diurnal cycle of precipitation than that of ERA5 over Amazonian region where propagating convective systems occur (Song and Zhang 2017).

Over East Asia, IMERG exhibits distinct features of afternoon and nocturnal-to-early-morning rainfall peaks in different subregions (Fig. 3e). In comparison with ERA5, QU-120 km better captures the nocturnal-to-early-morning peaks downstream of the Tibetan Plateau over the land and shows increased diurnal amplitude over the East China Sea (Fig. 3f–g). The distinct diurnal features over certain regions are properly distinguished by the model, including the late-afternoon peaks over southern China and nocturnal peaks over the southern slopes of the Tibetan Plateau (Fig. 3g). VR-EA exhibits a more inhomogeneous pattern of the diurnal cycle of precipitation over the refinement region that is less smooth than that in QU-120 km (Fig. 3h). When the resolution is refined, the topographic gradient becomes more realistic, and the dynamical and physical processes are better resolved.

In the transition zone of the VR mesh, no artificial pattern in terms of the local time peak and amplitude of precipitation diurnal cycle is found in the VR simulation (Fig. 3h). VR-EA generally presents late-afternoon peak over the main body of the Tibetan Plateau although the peak phase is slightly earlier than that of IMERG. The model captures the late-afternoon peak over India and the nocturnal-to-early-morning peak over the northwestern Bay of Bengal. In comparison with ERA5, VR-EA reproduces more realistic features of diurnal cycle over the Maritime Continent (Fig. 3d). The diurnal features produced by VR-EA and QU-120 km are overall close in the transition zone (Fig. 3g–h).

Several representative regions with typical features on the diurnal cycle of precipitation located in the refinement region, transition zone (denoted by boxes in Fig. 1) and coarse-resolution region are further studied. The regionally averaged results over these regions are shown in Fig. 4. In the refinement region, VR-EA generally exhibits a better performance than QU-120 km, although the model sensitivity to resolution might be different depending on each specific subregion. Over central eastern China, VR-EA shows substantial increase in amplitude in comparison

Table 1 Root mean square error (RMSE) and spatial correlation coefficient (SCC) of precipitation between IMERG and ERA5/QU-120 km/VR-EA over the refinement region, transition zone, and coarse-resolution region

Data source	Refinement region		Transition zone		Coarse-resolution region	
	RMSE	SCC	RMSE	SCC	RMSE	SCC
ERA5	1.62	0.88	1.64	0.91	1.08	0.92
QU-120 km	2.16	0.77	2.24	0.87	1.26	0.88
VR-EA	1.92	0.82	1.99	0.90	1.20	0.89

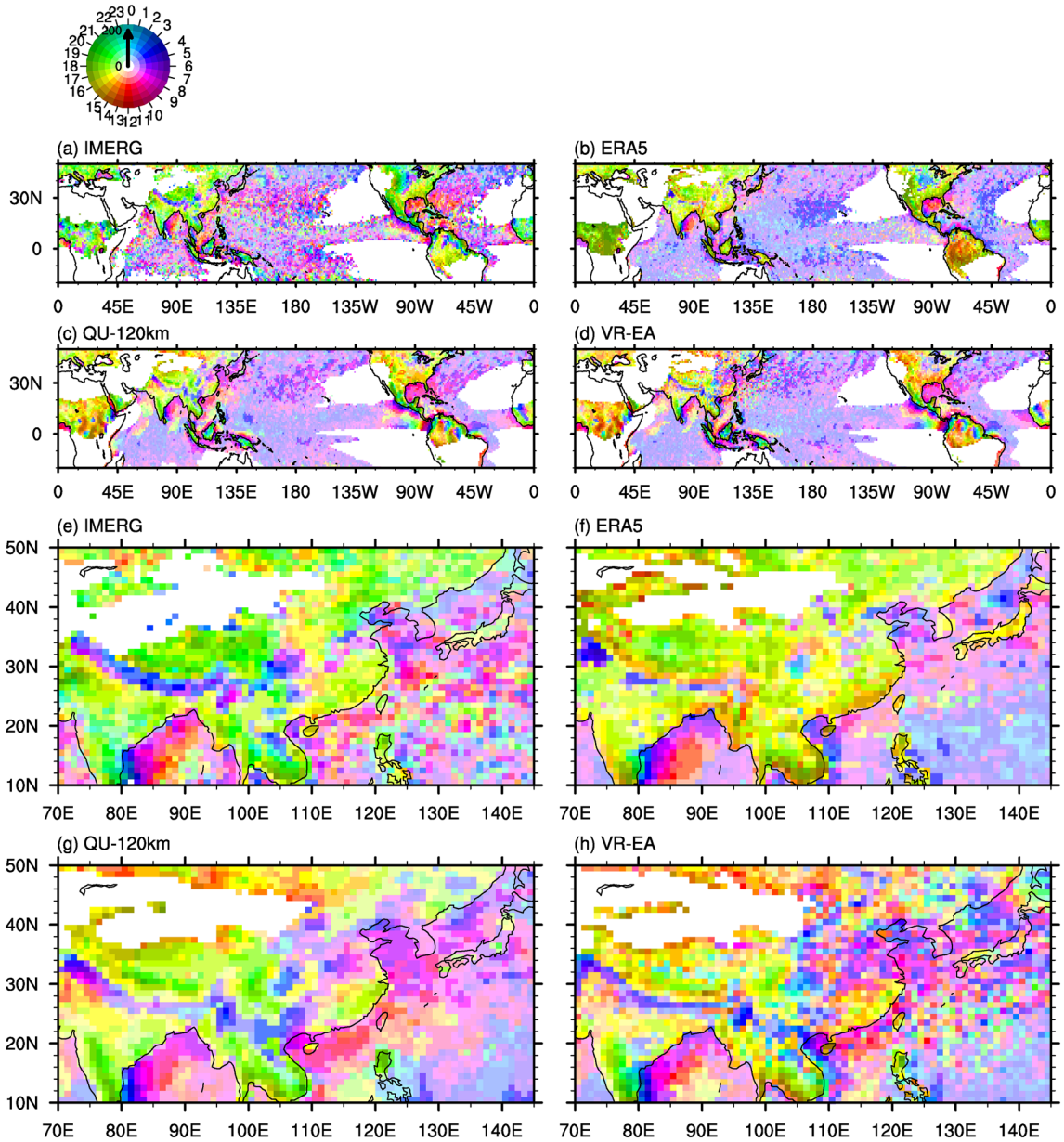

Fig. 3 Local time peak (color hue; unit: h) and amplitude (color saturation; unit: dimensionless) of the diurnal cycle of total precipitation rates during JJA for **a** IMERG, **b** ERA5, **c** QU-120 km, and **d** VR-EA. **e**–**h** Same as **a**–**d** but zoomed in for East Asia in the refinement region and part of the transition zone. Areas in which the JJA mean precipitation is < 1 mm/day are masked

with QU-120 km. Over central western China, as the local resolution increases from 120 to 35 km, the amplitude of the diurnal cycle becomes smaller over regions of high topography (Fig. 4b) and larger over regions of low topography (Fig. 4c). Such resolution sensitivity is related to the moving precipitating systems developed from the high mountains (see Zhang et al. 2021). VR-EA well captures the eastward-propagating nighttime systems and reduces the overly strong late-afternoon rainfall rates. Over southern China, VR-EA produces larger afternoon precipitation than QU-120 km, getting closer to the observations.

Outside the refinement region, VR-EA also performs well in certain representative regions. For the transition zone, the model well captures the diurnal cycle over India, although the peak time is slightly earlier than that seen in the observations (Fig. 4e). Mesh refinement could result in artificial wave distortion and reflection in the transition zone where the mesh resolution varies. Such artificial dynamical forcing may deteriorate the performance in simulating diurnal cycle of

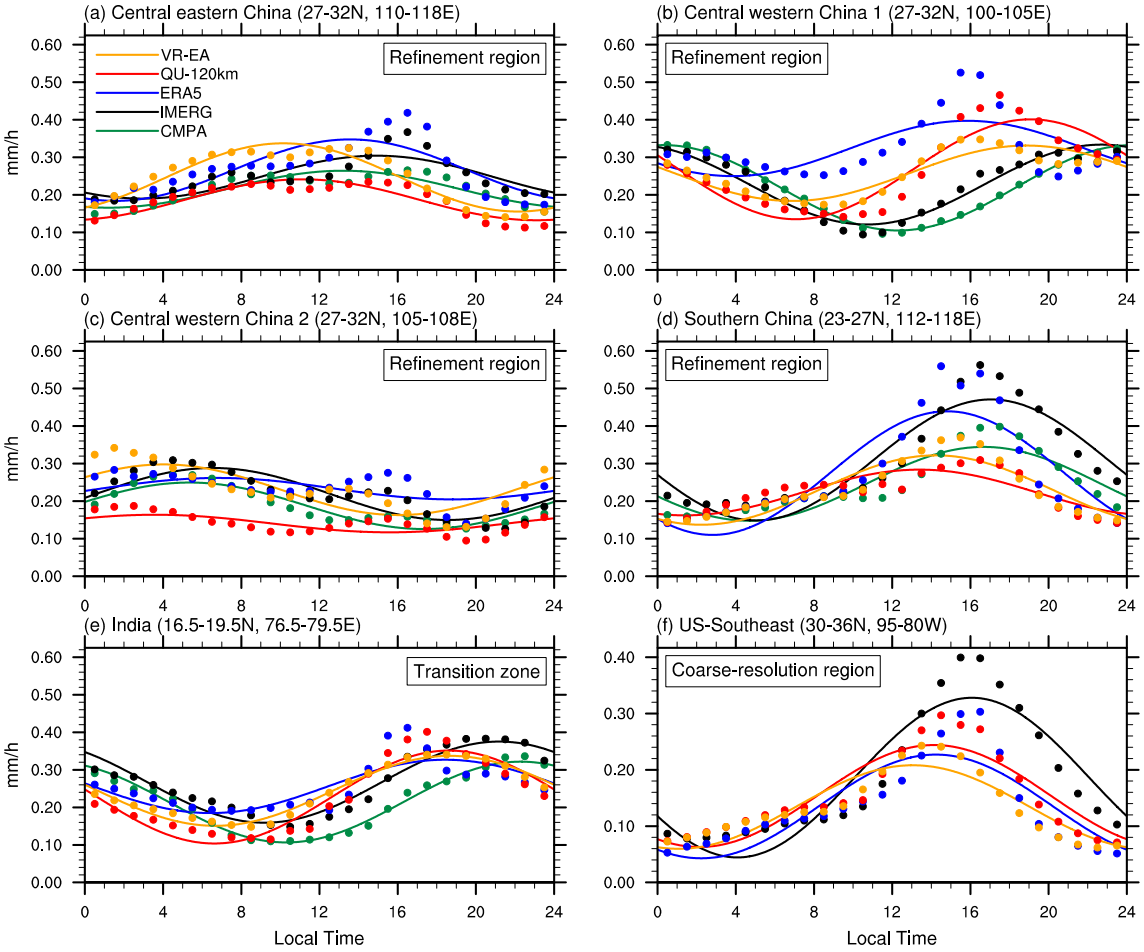

Fig. 4 Diurnal cycle of precipitation rate (dot) and its first harmonic component (solid line) during JJA over the regions in **a** central eastern China (CEC), **b** central western China on the lee side of the Tibetan Plateau with high topography (CWC1) and **c** downstream of the Tibetan Plateau with low topography (CWC2), **d** southern China (SC), **e** India (IND), and **f** southeast U.S. Regionally averaged precipitation is given for each subregion. For the VR mesh, the four regions in China are located in the refinement region, the region of India is located in the transition zone, and the southeast U.S. is located in the coarse-resolution region

precipitation. However, VR-EA does not show artificial signals in terms of the rainfall diurnal feature (i.e., overall consistent peak time and amplitude of precipitation diurnal cycle with those of IMERG) that might be caused by varying grid spacing. Overall, the discrepancies among the model simulations and observations are small. For the coarse-resolution region, both QU-120 km and VR-EA capture the afternoon peak time over the southeast U.S. (Fig. 4f). The modeled rainfall peak time and the first harmonic component of the diurnal cycle are broadly consistent with those of IMERG.

4 Dynamics–physics interaction

Previous analyses have revealed different responses in the diurnal cycle of precipitation to model resolution over different regions. GRIST reproduces the distinct features of the diurnal cycle over East Asia. To understand whether the diurnal features are generated by reasonable precipitation processes, we further investigate the dynamics–physics interaction. This analysis is performed in terms of both the resolved and the sub-resolved scale. The daytime and nighttime rainfall peaks are generally caused by different precipitation processes. The two types of diurnal rainfall peaks represent key dynamic and thermodynamic processes, which serve as effective indicators to understand model behaviors of precipitation generation. We selected central eastern China (27°–32° N, 110°–118° E) as a representative region characterized by nocturnal-to-early-morning and late-afternoon rainfall peaks (Fig. 5a). Central western China downstream of the Tibetan Plateau (27°–32° N, 105°–108° E) was selected as a typical continental region characterized by a nocturnal rainfall peak for comparison of resolution sensitivity. The dynamical and thermodynamical conditions are examined to verify

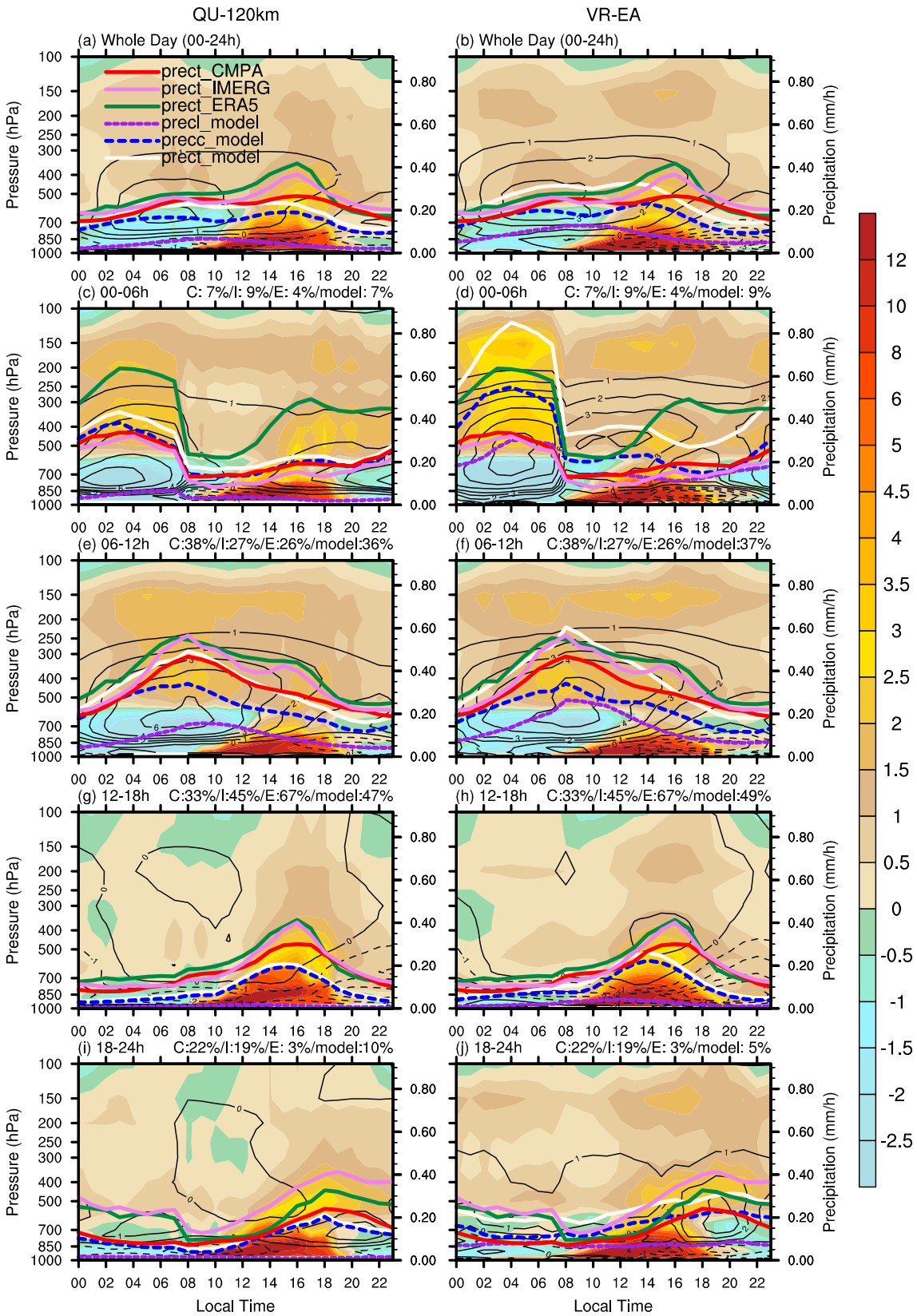
QU-120km
VR-EA
(a) Whole Day (00-24h)
(b) Whole Day (00-24h)
prect_CMPA
prect_IMERG
prect_ERA5
precl_model
precc_model
prect_model
(c) 00-06h C: 7%/I: 9%/E: 4%/model: 7%
(d) 00-06h C: 7%/I: 9%/E: 4%/model: 9%
(e) 06-12h C:38%/I:27%/E:26%/model:36%
(f) 06-12h C:38%/I:27%/E:26%/model:37%
(g) 12-18h C:33%/I:45%/E:67%/model:47%
(h) 12-18h C:33%/I:45%/E:67%/model:49%
(i) 18-24h C:22%/I:19%/E: 3%/model:10%
(j) 18-24h C:22%/I:19%/E: 3%/model: 5%
Pressure (hPa)
Precipitation (mm/h)
Local Time

◂**Fig. 5** Composited heating rates $Q_1 - Q_2 - Q_R$ (filled contours; K/day), scaled vertical advection of water vapor (thin black lines; K/day) and precipitation rates (thick colored curves; mm/h) over central eastern China (27°–32° N, 110–118° E) based on the peak-time phases of total precipitation rates: **a**, **b** the entire day, **c**, **d** 0000–0600 LST, **e**, **f** 0600-1200 LST, **g**, **h** 1200–1800 LST, and **i**, **j** 1800–2400 LST. Solid colored lines denote the total precipitation rates of CMPA (red), IMERG (violet), ERA5 (green), and the model (white). Model simulations include QU-120 km (left column) and VR-EA (locally 35 km; right column). Dotted blue (dashed purple) line represents the convective (large-scale) precipitation rates in the model simulation. Percentages of certain peak-time type for CMPA (C), IMERG (I), ERA5 (E), and the model (quasi-uniform or variable-resolution simulation) data are listed to the right above each subplot. Numbers on the horizontal axis denotes the time half an hour later (e.g., "00" represents the actual time of "00:30")

the model capability in reproducing realistic precipitation processes.

4.1 Different physical mechanisms related to daytime and nighttime rainfall peaks

Over central eastern China, in comparison with CMPA, both IMERG and ERA5 have larger rainfall amounts in the afternoon. The two GRIST simulations reproduce the two peaks of the diurnal cycle, as seen in CMPA. The precipitation rates of QU-120 km are generally weaker than those of the observations and ERA5 (Fig. 5a). With refinement of the resolution, VR-EA exhibits larger precipitation rates throughout the day (Fig. 5b). During midnight to early morning, upper-level positive and lower-level negative $Q_1 - Q_2 - Q_R$ indicates a convective structure with maximum subgrid-scale transport of moist static energy (Tang and Zhang 2015) at ~ 600 hPa. Under the circumstance that a low-level (below 850 hPa) cooling and mid-level (300–700 hPa) heating stratiform structure dominates diabatic heating pattern (Fig. 6a, b), the mid-level heating and upward vertical moisture transport become intensified in the early morning. The representation of both afternoon convective heating and early morning stratiform heating corresponds to the diurnal cycle of precipitation, suggesting that the model can simulate precipitation in a reasonable manner.

To identify the specific characteristics of the precipitation processes, we composited the precipitation and diagnostic variables based on the four peak time phases. In CMPA, the early morning peak during 0600–1200 LST (38%) and the afternoon peak during 1200–1800 LST (33%) dominate the diurnal cycle. The composited precipitation and diagnostics exhibit fundamentally different precipitation processes of the two peaks. The nocturnal-to-early-morning rainfall is controlled by large-scale forcing and it exhibits a dominate response to upward moisture advection. The afternoon peak is mainly caused by surface-heating induced convective activity, where grid-scale forcing is weak while subgrid-scale diabatic heating dominates. The peaks during 0000–0600 LST and 1800–2400 LST can be regarded as atypical realization of the two major types of rainfall peak.

For the 0000–0600 LST phase, in comparison with QU-120 km, the rainfall and mid-level heating are markedly intensified during the night in VR-EA (Fig. 5c, d). The large increment in large-scale precipitation of VR-EA is mainly attributed to the favorable dynamical lifting condition. The change attributable to the refined resolution not only contributes to the increment in the climatological mean nocturnal rainfall, but also enhances the mean large-scale precipitation in the afternoon. The peak time during 0600–1200 LST dominates in CMPA (Fig. 5e). In comparison with QU-120 km, the maximum rainfall rate is increased in VR-EA, which is contributed by large-scale precipitation (Fig. 5f). The mid-level heating is intensified around 500 hPa owing to condensation, which plays an important role in providing a more realistic environment (Fig. 6f). VR-EA reproduces a suitable large-scale dynamical condition for the nocturnal-to-early-morning rainfall.

Peak time during 1200–1800 LST dominates in IMERG and ERA5, as well as both model simulations (Fig. 5g–h). The model well captures the mechanism of precipitation generation with regard to the convective activity. In comparison with QU-120 km, the convective activity and precipitation are intensified in VR-EA. The maximum rainfall rate of VR-EA is increased and approaches that of the observations. This partly contributes to the increased amount of its climatological mean afternoon precipitation. For the 1800–2400 LST phase, nighttime precipitation and the mid-level heating due to condensation strengthen as the resolution increases from QU-120 km to VR-EA (Figs. 5i–j, 6i–j).

As shown in the composited results, the model can simulate two different mechanisms of precipitation generation related to the early morning peaks and the afternoon peaks. Meanwhile, the percentages of the 0000–1200 LST phase (sum of the 0000–0600 and 0600–1200 LST phases) and the 1200–2400 LST phase (sum of the 1200–1800 and 1800–2400 LST phases) peaks in the model are reasonably close to those of CMPA. Thus, the climatological mean diurnal cycle of precipitation of the model is comparable with that of the observations. Although GRIST shows some advantages in the aforementioned aspects, it still has some deficiencies in reproducing the climate statistics. The majority of precipitation generated by the model during 1200–2400 LST is in the afternoon (1200–1800 LST). The underlying reason may be associated to the convective scheme that contributes to earlier trigger of convection.

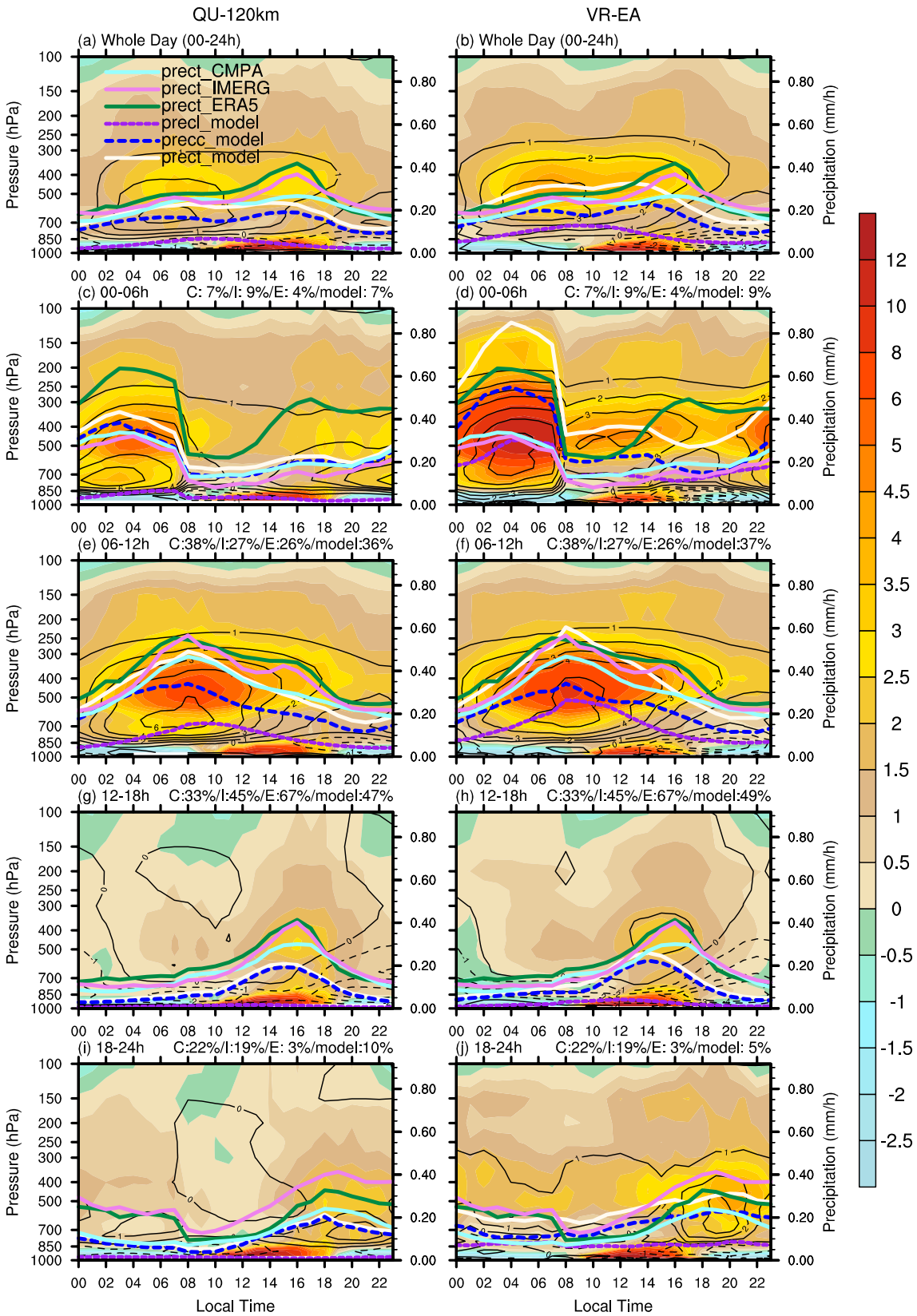

Fig. 6 Same as Fig. 5, but the composited heating rates are replaced by $Q_1 - Q_R$ (filled contours; K/day) and light blue lines denote the total precipitation rates (mm/h) of CMPA

4.2 Impacts of large-scale dynamical forcing on nocturnal rainfall events

Over central western China downstream of the Tibetan Plateau, nocturnal rainfall dominates in CMPA and IMERG (Fig. 7a). A subpeak in the rainfall rate is found in the afternoon, although its magnitude is not as large as the nighttime peak. Both QU-120 km and VR-EA reproduce these major features of the diurnal cycle of precipitation (Fig. 7a, b). Rainfall intensity is weaker in QU-120 km than in the observations. With increasing resolution, the rainfall becomes intensified in VR-EA. For the 0000–0600 LST phase, both the two simulations show a pattern of low-level cooling and mid-level heating at night (Fig. 7e–h). The nocturnal rainfall amount increases and the mid-level heating strengthens when the local resolution increases from QU-120 km to VR-EA. The frequency also increases slightly but is generally comparable with that in the observations. The 0600–1200 LST phase dominates in CMPA and IMERG (42% and 37%). In comparison with QU-120 km, VR-EA clearly produces more precipitation in the early morning, which is closer to the observations (Figure not shown). For the 1200–1800 LST phase, the nocturnal rainfall amount is largely reduced owing to weaker large-scale forcing in both simulations (Fig. 7i–l).

To verify the model behavior in capturing the dynamical condition of the nocturnal precipitation peak, we investigated the local divergence structure by comparing ERA5 and the VR-EA simulation. ERA5 presents strong convergence at low levels (around 850 hPa) and weak divergence at upper levels (around 600 hPa) from late night to early morning (Fig. 8a). VR-EA exhibits a similar circulation structure although the magnitudes of the convergence and divergence are larger (Fig. 8b). Such a dynamical structure leads to strong ascending motion at 700 hPa, strengthening the vertical moisture advection (Fig. 7). We composited the divergence of ERA5 on the early morning peak (0000–0600 LST) days of CMPA precipitation data. In the composite phase, low-level convergence is strengthened at midnight in comparison with the climatological mean state (Fig. 8c). The upper-level divergence extends from 600 to 100 hPa. In the composite phase of VR-EA, both the convergence and the divergence become stronger (Fig. 8d). The composite dynamical structure implies favorable conditions for nocturnal precipitation occurrence.

The thermal environment can also be affected by large-scale dynamical forcing. We further examine the thermal

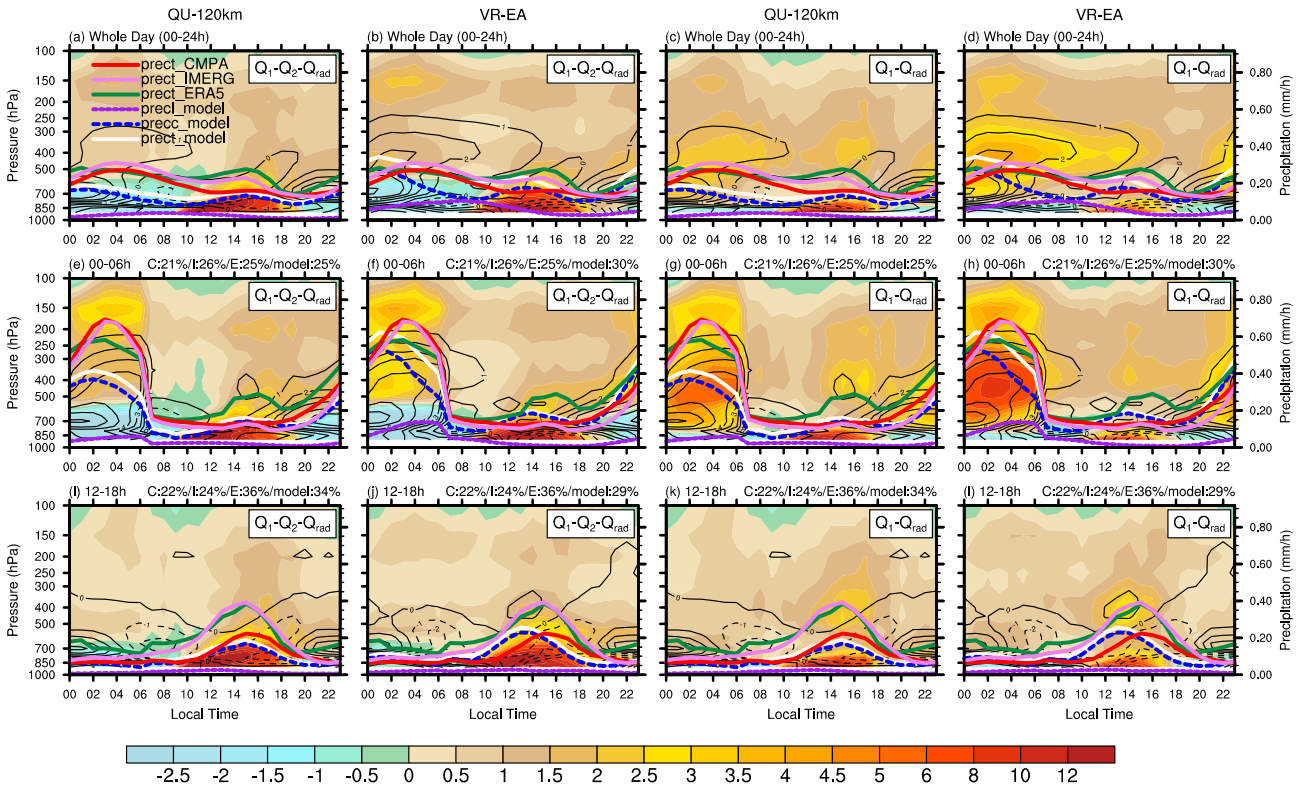

Fig. 7 Same as Fig. 5, but for central western China downstream of the Tibetan Plateau (27°–32° N, 105°–108° E). Filled contours denote $Q_1 - Q_2 - Q_R$ (K/day) in the two left columns and $Q_1 - Q_R$ (K/day) in the two right columns. Only the **a**–**d** climatological mean, the **e**–**h** 0000–0600 LST phase, and the **i**–**l** 1200–1800 LST phase are shown

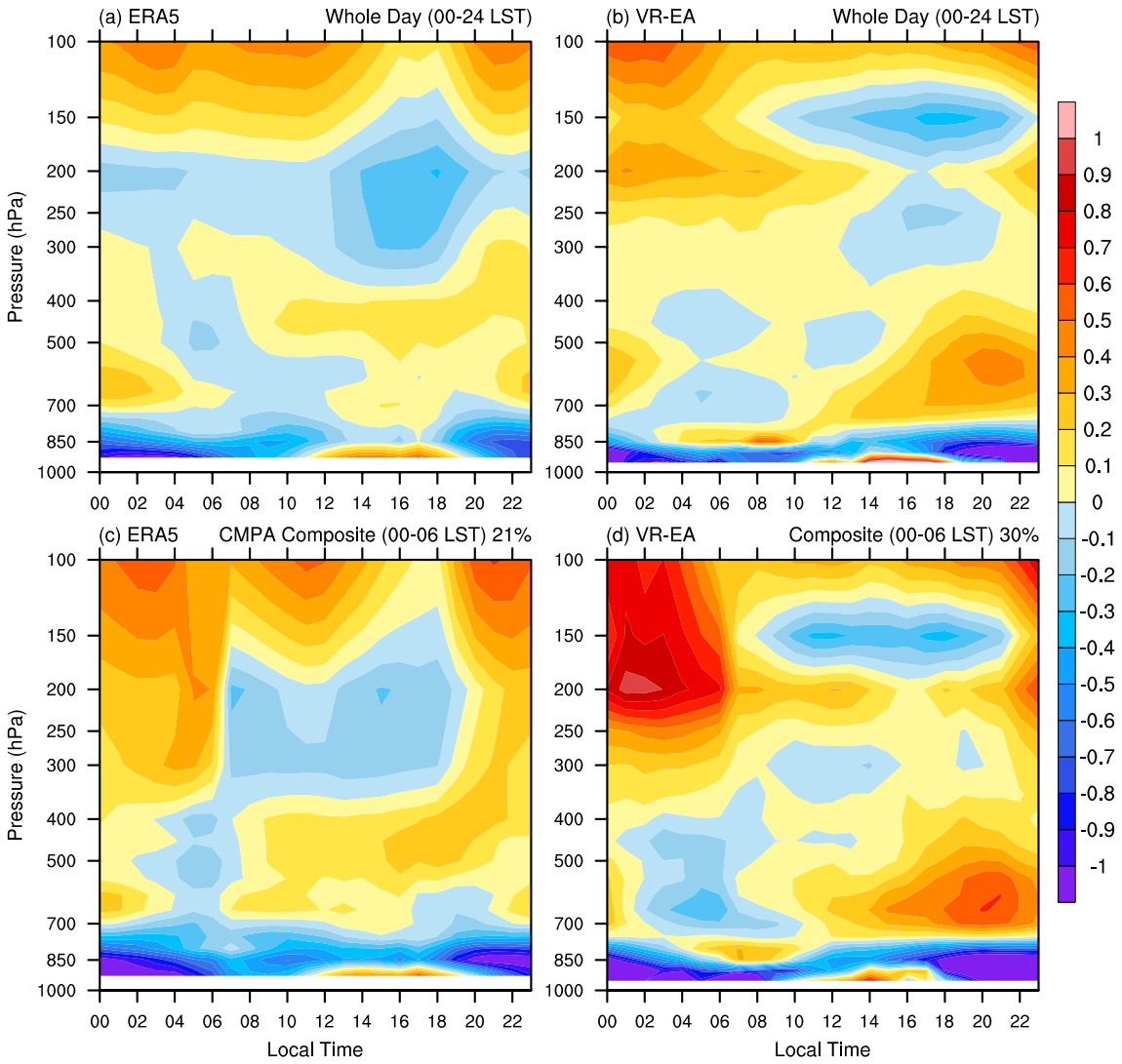

Fig. 8 **a**, **b** Climatological mean and **c**, **d** composited divergence ($10^{-5}\,s^{-1}$) on the early morning rainfall peak (during 0000–0600 LST) days over central western China downstream of the Tibetan Plateau (27°–32° N, 105°–108° E) in ERA5 and VR-EA. The selected days for the composited divergence of ERA5 are based on CMPA precipitation data. The percentages of the 0000–0600 LST phase for **c** CMPA and **d** VR-EA are presented to the right above each subplot

condition related to the large-scale circulation for nocturnal rainfall. As shown in Fig. 9a, a southerly wind induces warm advection at 700 hPa downstream of the Tibetan Plateau at midnight. We composited the potential temperature advection and wind of ERA5 (0.25° × 0.25° grid data) on early morning (0000–0600 LST) and afternoon (1200–1800 LST) peak days of CMPA precipitation data. For the 0000–0600 LST phase, warm advection is intensified owing to anomalous southwesterlies (Fig. 9c). VR-EA represents the variation of warm advection in this phase similar to that of ERA5 (Fig. 9b, d). The warm advection corresponds to strong lower-level convergence and provides a stimulus for enhancement of ascending motion at 700 hPa. For the 1200–1800 LST phase, ERA5 and VR-EA both present anomalous easterlies that weaken the warm advection (Fig. 9e, f). The large-scale forcing is not as strong as that in the early morning peak phase and the nocturnal rainfall amount is largely reduced (Fig. 7h, l). The anomalous southwesterlies (easterlies) in the 0000–0600 LST phase (1200–1800 LST phase) represent the strengthening (weakening) of Asian summer monsoon (Chen 2020). The different background flows modulate the diurnal cycle of precipitation downstream of the Tibetan Plateau, which are clearly simulated by the model.

The southwesterlies not only bring low-level warm advection, but also transport warm moist air toward middle levels over central western China downstream of the Tibetan Plateau. The climatological mean cold advection at

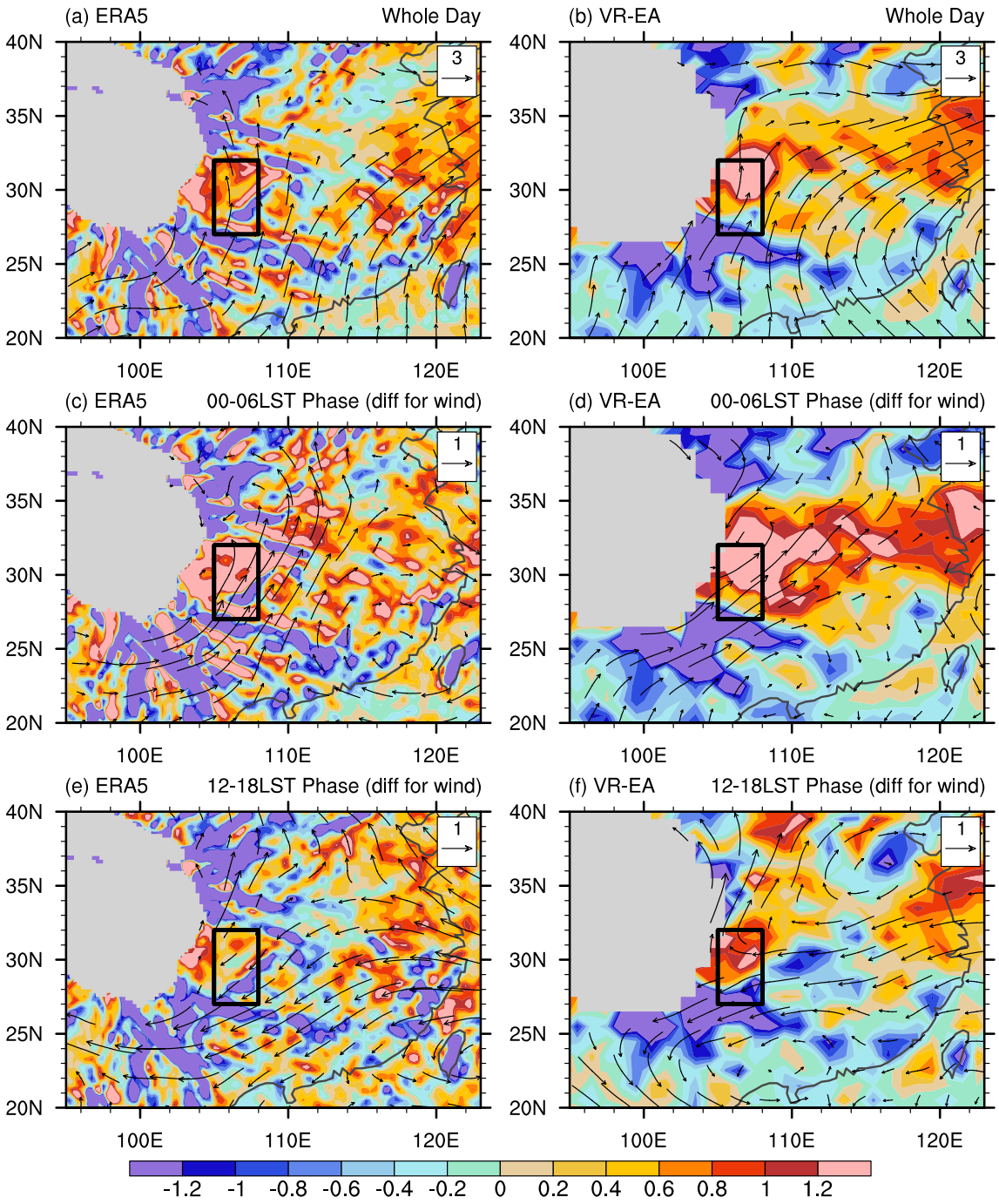

Fig. 9 **a**, **b** Climatological mean and **c**, **d** composited potential temperature advection (filled contours; K/day) and wind (vector; m/s) at 700 hPa on early-morning rainfall peak (during 0000–0600 LST) days over central western China downstream of the Tibetan Plateau (27°–32° N, 105°–108° E) in ERA5 (left column) and VR-EA (right column) at 0000 BJT (Beijing Time; local time at 120° E). The days selected for the composited temperature advection and wind of ERA5 were based on CMPA precipitation data. In **c**–**d**, the vector denotes the difference in wind between the composite and the climatological mean. **e**–**f** Same as **c**–**d** but for the composite results on afternoon rainfall peak (during 1200–1800 LST) days. Black boxes mark the region for the precipitation analysis (27°–32° N, 105°–108° E)

400–500 hPa dominates the lee side of the Tibetan Plateau where the westerlies prevail (Fig. 10a). For the 0000–0600 LST phase, the anomalous southwesterlies exist at the middle level, consistent with the anomalous wind field at the lower level (Figs. 9c, 10c). The anomalous southwesterlies induce weak warm advection at 400–500 hPa. The transportation of warm moist air in the middle and low levels from the southwest facilitates strong ascending motion and

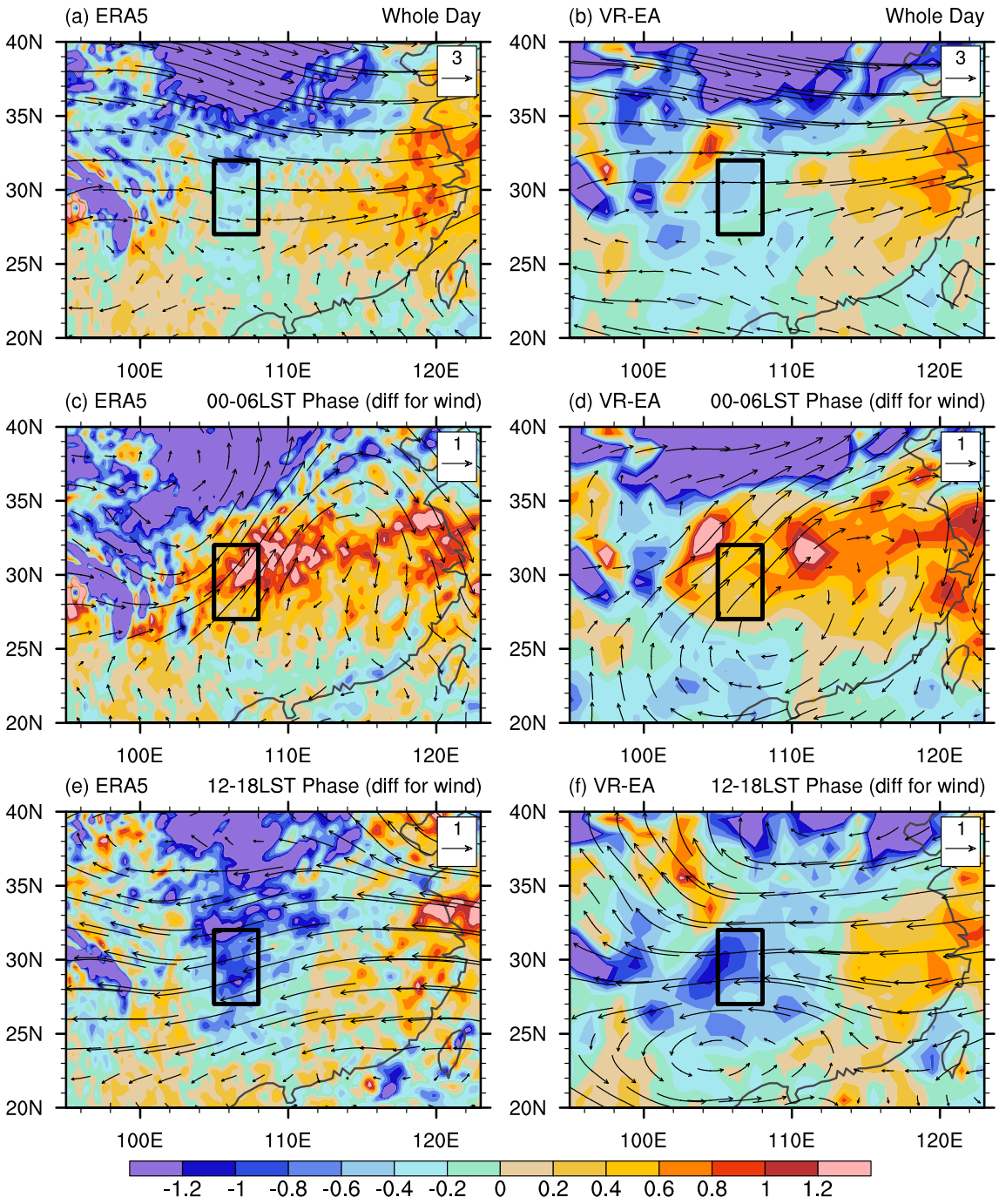

Fig. 10 Same as Fig. 9, but for the potential temperature advection and wind at 400–500 hPa (layer-averaged)

brings abundant water vapor (Fig. 7h). VR-EA captures the anomalous southwesterlies and the induced thermal advection in the composite phase, which contribute to the intense nocturnal rainfall under the favorable dynamical conditions. In the 1200–1800 LST phase, differences in the anomalous winds between ERA5 and VR-EA exist in southwest China at lower latitude within 20°–24° N (Fig. 10e, f). The anomalous governing circulation of easterlies and the induced cold advection over central western China downstream of the Tibetan Plateau in VR-EA is consistent with those of ERA5.

4.3 Eastward propagating precipitation process

The composite results based on the diurnal rainfall peak time demonstrates that the model well captures different physical mechanisms of precipitation generation. The composite

analysis also reveals the influence of dynamical forcing on nocturnal rainfall events. The previous analysis is mainly based on the statistical features, which limits the understanding of the difference between the quasi-uniform and VR models. To understand the model sensitivity to resolution in a process level, we further investigate the model ability to reproducing eastward propagating precipitation processes downstream of the Tibetan Plateau. A typical case of extreme precipitation event with eastward movement of the southwest vortex during the midsummer of 2016 is selected (Li et al. 2018). We conducted 3-day simulations started at 0000 UTC on 29 June 2016 based on the QU-120 km and VR-EA model. Other model configurations of the two simulations are consistent with their own AMIP experiments.

In CMPA, precipitation exhibits an eastward-delayed diurnal phase downstream of the Tibetan Plateau (Fig. 11a). Heavy rainfall starts at 0200 BJT 30 June over central western China (27°–32° N, 105°–108° E) and then moves towards the Yangtze River valley. QU-120 km generally captures the eastward propagating feature although the speed of the propagation is slower than the observation (Fig. 11b). In comparison with QU-120 km, VR-EA better simulates the propagation process in term of the speed and the precipitation system moves a longer distance towards the Yangtze River valley (Fig. 11c). The precipitation rate also increases as the model resolution is refined. It should be noted that it is the intercomparison between the two simulations that can provide a reference for understanding the model sensitivity, while the absolute value of precipitation rate of the model in such a case study is of secondary interest.

During the period from 0200 LST 30 June to 0200 LST 1 July, upper-level positive and lower-level negative $Q_1 - Q_2 - Q_R$ indicates a deep convective structure associated with the eastward-propagating convective system (Fig. 12). In QU-120 km, convective precipitation dominates the total rainfall from 0200 to 1100 LST. At the peak time of 1400 LST, large-scale precipitation rate largely contributes to the total rainfall rate. As the resolution is refined, VR-EA

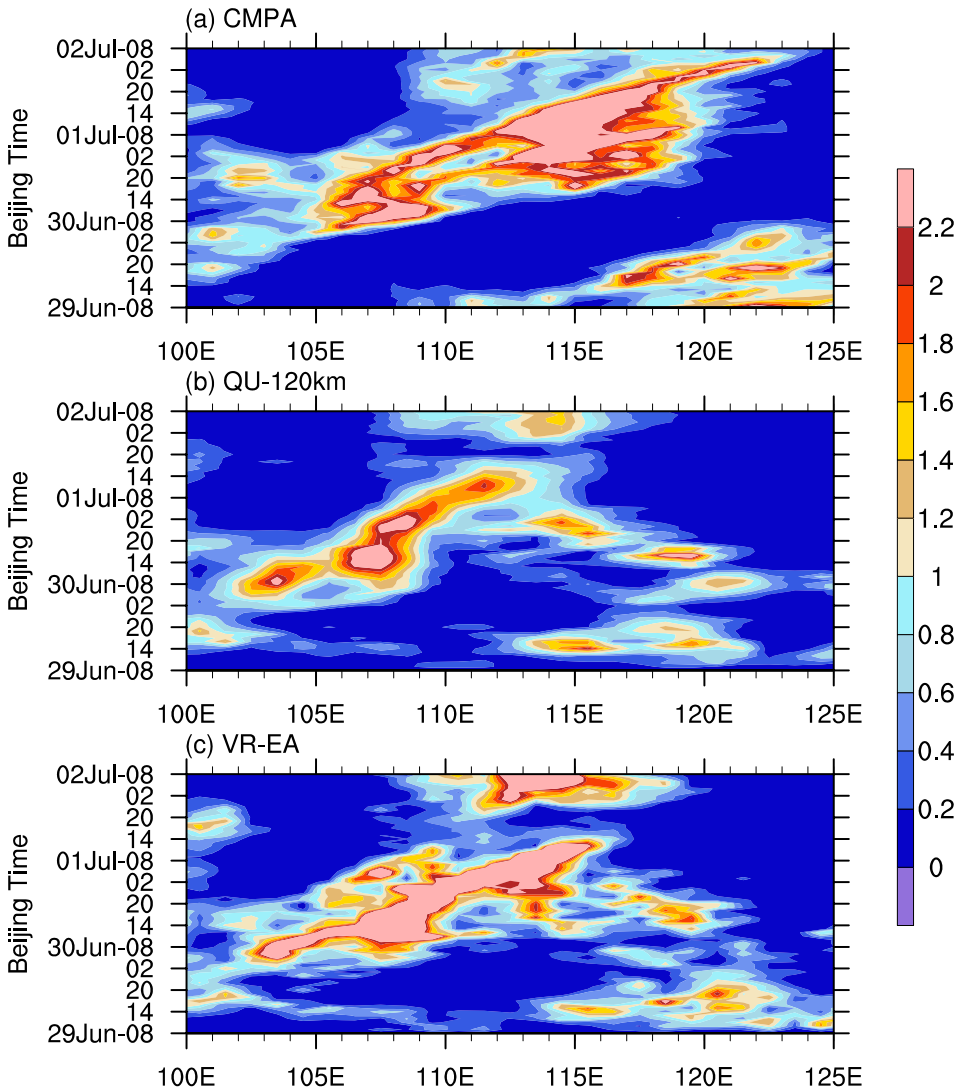

Fig. 11 Time-longitude diagrams of precipitation (mm/h) over East Asia (averaged over 27°–32° N) for **a** CMPA, **b** QU-120 km, and **c** VR-EA during the eastward propagating precipitation event (29 June–2 July 2016)

presents a similar variation in the ratio of convective and large-scale precipitation rate to total precipitation rate. In comparison to QU-120 km, the large-scale precipitation rate is larger at the peak time when vertical convergence of eddy transport of total heat (400–500 hPa) and upward moisture advection become stronger in VR-EA. Such model sensitivity to resolution is generally consistent to that of the climate statistics.

5 Conclusion and discussion

This study examines the GRIST-NWP model in simulating the diurnal cycle of precipitation at relatively coarse horizontal resolutions. The global performance is evaluated in terms of the refinement region, transition zone, and coarse-resolution region. Composited dynamic, thermodynamic, and moisture conditions are diagnosed to analyze the impact of model dynamics and physics on the diurnal features. The main conclusions can be summarized as follows.

Overall, GRIST reproduces the global features of the diurnal cycle of precipitation. The discrepancy in rainfall peak time between the late-afternoon peaks dominating over the land and nocturnal-to-early-morning peaks dominating over the ocean is well simulated. The model captures the distinct regional features at different geographical locations. The VR simulation exhibits more inhomogeneous patterns in comparison with the uniform-resolution one in the refinement region. Although model sensitivity to resolution is unique over each region, VR-EA generally reproduces more consistent diurnal rainfall features in terms of peak phase and amplitude with those of the observations over certain regions of China in comparison to QU-120 km. No apparent artificial features are observed

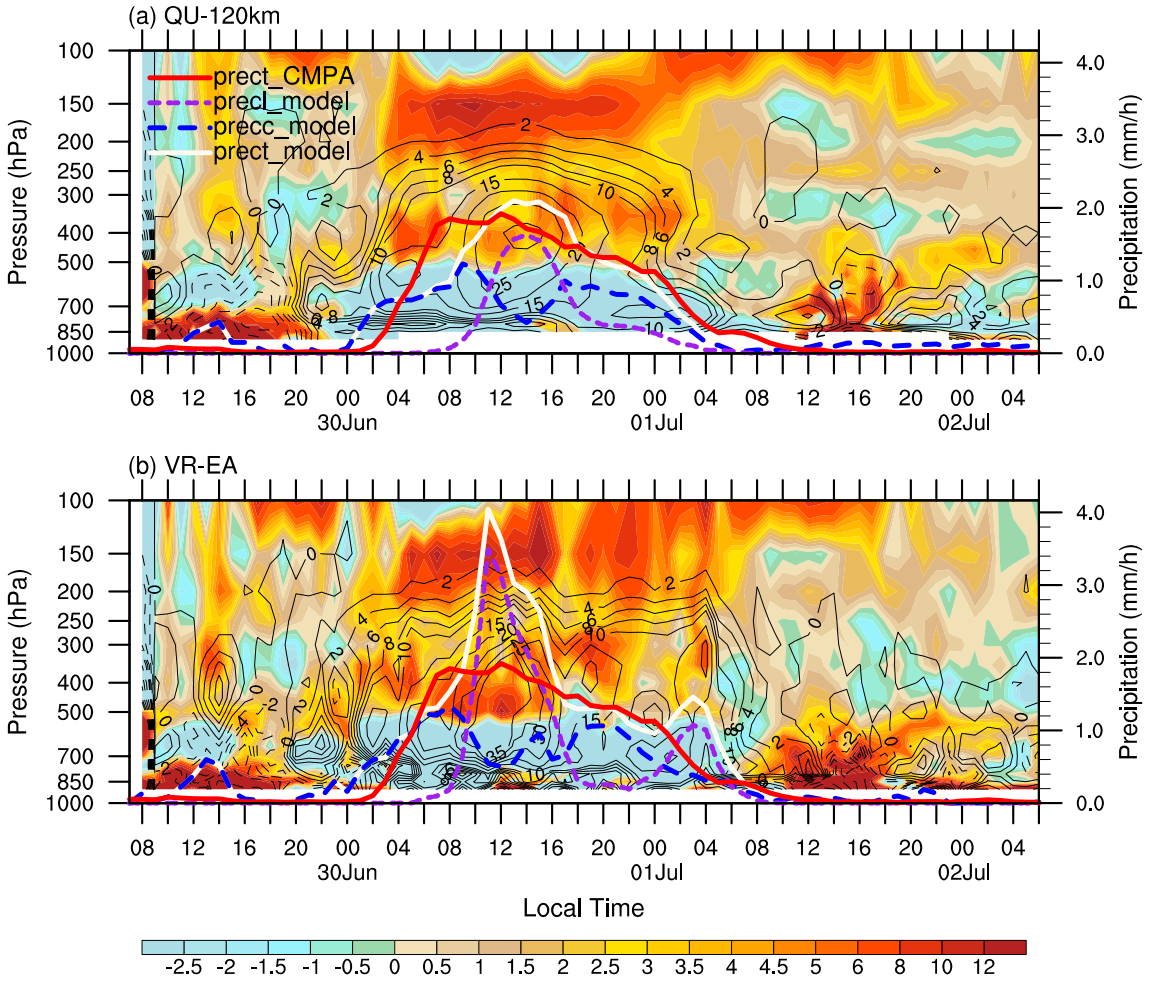

Fig. 12 Heating rates $Q_1 - Q_2 - Q_R$ (filled contours; K/day) and scaled vertical advection of water vapor (thin black lines; K/day) in **a** QU-120 km and **b** VR-EA over central western China (27°–32° N, 105–108° E) during the eastward propagating precipitation event (29 June–2 July 2016). Solid colored lines denote the total precipitation rates (mm/h) of CMPA (red) and the model (white). Dotted blue (dashed purple) line represents the convective (large-scale) precipitation rates (mm/h) in the model simulation. Numbers on the horizontal axis denotes the time half an hour later (e.g., "00" represents the actual time of "00:30")

in the transition zone of the VR meshes. In the coarse-resolution region, VR-EA represents similar features to QU-120 km.

GRIST can distinguish different types of precipitation processes through reasonable dynamics–physics interaction over East Asia. Composited diagnostics of the phase of the four peak times shows clear differences in the mechanism of precipitation generation between daytime and nighttime peaks. The model captures the dominant contribution of large-scale forcing to stratiform-like rainfall peaks and produces daytime surface-heating induced rainfall over central eastern China. Refining the local resolution increases the composited precipitation rates at night, which become comparable with the observations over central western China. In the 0000–0600 LST phase, the composited low-level convergence and upper-level divergence at night become stronger and the strengthened southwesterlies transport warm moist air toward the low and middle levels downstream of the Tibetan Plateau. The model reasonably simulates the dynamical and thermodynamical conditions for the occurrence of nocturnal rainfall.

Although the GRIST model exhibits good performance in simulating the diurnal cycle of precipitation in the above aspects, some remaining model deficiencies are still found. The model simulates an earlier afternoon peak time over the land (e.g., North America) than that in the observations. Modified convection scheme and/or convective-permitting modeling may provide a way for improving the simulation.

Acknowledgements This research was supported by National Natural Science Foundation of China (41875135). The authors highly appreciate the comments from two reviewers.

Author contributions YihZ performed the data analysis, prepared all figures, and wrote the manuscript. RY and YiZ designed the research and revised the manuscript. JL revised the manuscript. All the authors discussed the results and approved the final manuscript.

Funding This research was supported by National Natural Science Foundation of China (41875135).

Data Availability The experimental data of GRIST for supporting this study are available in the Zenodo repository at https://zenodo.org/record/7336401. The Integrated Multisatellite Retrievals for GPM (IMERG) data were obtained from the Goddard Earth Sciences Data and Information Services Center (GES DISC) and area available online at https://gpm1.gesdisc.eosdis.nasa.gov/data/GPM_L3/GPM_3IMERGHH.06. The ERA5 reanalysis data were obtained from the Copernicus Climate Change Service (C3S) Climate Data Store (CDS) and area available online at https://cds.climate.copernicus.eu.

Declarations

Conflict of interest The authors declare that there is no conflict of interest.

References

Bechtold P, Chaboureau JP, Beljaars A, Betts AK, Kohler M, Miller M, Redelsperger JL (2004) The simulation of the diurnal cycle of convective precipitation over land in a global model. Q J R Meteorol Soc 130:3119–3137. https://doi.org/10.1256/qj.03.103

Bechtold P, Köhler M, Jung T, Doblas-Reyes F, Leutbecher M, Rodwell MJ, Vitart F, Balsamo G (2008) Advances in simulating atmospheric variability with the ECMWF model: from synoptic to decadal time-scales. Q J R Meteorol Soc 134:1337–1351. https://doi.org/10.1002/qj.289

Bechtold P, Sandu I, Klocke D, Semane N, Ahlgrimm M, Beljaars A, Forbes R, Rodwell M (2014a) The role of shallow convection in ECMWF's integrated forecasting system. European Centre for Medium-Range Weather Forecasts

Bechtold P, Semane N, Lopez P, Chaboureau JP, Beljaars A, Bormann N (2014b) Representing equilibrium and nonequilibrium convection in large-scale models. J Atmos Sci 71:734–753. https://doi.org/10.1175/Jas-D-13-0163.1

Chen G (2020) Diurnal cycle of the Asian Summer Monsoon: air pump of the second kind. J Clim 33:1747–1775. https://doi.org/10.1175/jcli-d-19-0210.1

Christopoulos C, Schneider T (2021) Assessing biases and climate implications of the diurnal precipitation cycle in climate models. Geophys Res Lett 48:e2021GL09301. https://doi.org/10.1029/2021GL093017

Collins WD, Rasch PJ, Boville BA, Hack JJ, McCaa JR, Williamson DL, Kiehl JT, Briegleb B (2004) Description of the NCAR Community Atmosphere Model (CAM 3.0)

Covey C, Gleckler PJ, Doutriaux C, Williams DN, Dai AG, Fasullo J, Trenberth K, Berg A (2016) Metrics for the diurnal cycle of precipitation: toward routine benchmarks for climate models. J Clim 29:4461–4471. https://doi.org/10.1175/Jcli-D-15-0664.1

Dai A (2001) Global precipitation and thunderstorm frequencies. Part II: diurnal variations. J Clim 14:1112–1128. https://doi.org/10.1175/1520-0442(2001)014<1112:Gpatfp>2.0.Co;2

Dirmeyer P, Cash B, Kinter J, Jung III, Marx T, Satoh L, Stan M, Tomita C, Towers H, Wedi P, Achuthavarier N, Adams D, Altshuler J, Huang E, Jin B, Manganello E J (2012) Simulating the diurnal cycle of rainfall in global climate models: resolution versus parameterization. Clim Dyn 39:399–418. https://doi.org/10.1007/s00382-011-1127-9

Fang Y, Wu P, Mizielinski M, Roberts M, Wu T, Li B, Vidale PL, Demory ME, Schiemann R (2017) High-resolution simulation of the boreal summer intraseasonal oscillation in Met Office Unified Model. Q J R Meteorol Soc 143:362–373. https://doi.org/10.1002/qj.2927

Feng Z, Song F, Sakaguchi K, Leung LR (2021) Evaluation of mesoscale convective systems in climate simulations: methodological development and results from MPAS-CAM over the United States. J Clim 34:2611–2633. https://doi.org/10.1175/jcli-d-20-0136.1

Gettelman A, Callaghan P, Larson VE, Zarzycki CM, Bacmeister JT, Lauritzen PH, Bogenschutz PA, Neale RB (2018) Regional climate simulations with the Community Earth System Model. J Adv Model Earth Syst 10:1245–1265. https://doi.org/10.1002/2017MS001227

Hashimoto A, Done JM, Fowler LD, Bruyère CL (2016) Tropical cyclone activity in nested regional and global grid-refined simulations. Clim Dyn 47:497–508. https://doi.org/10.1007/s00382-015-2852-2

Hersbach H, Bell B, Berrisford P, Hirahara S, Horányi A, Muñoz-Sabater J, Nicolas J, Peubey C, Radu R, Schepers D, Simmons A, Soci C, Abdalla S, Abellan X, Balsamo G, Bechtold P, Biavati G, Bidlot J, Bonavita M, De Chiara G, Dahlgren P, Dee D, Diamantakis M, Dragani R, Flemming J, Forbes R, Fuentes M, Geer A, Haimberger L, Healy S, Hogan RJ, Hólm E, Janisková M, Keeley S, Laloyaux P, Lopez P, Lupu C, Radnoti G, de Rosnay P, Rozum I, Vamborg F, Villaume S, Thépaut J-N (2020) The ERA5 global reanalysis. Q J R Meteorol Soc 146:1999–2049. https://doi.org/10.1002/qj.3803

Hohenegger C, Kornblueh L, Klocke D, Becker T, Cioni G, Engels JF, Schulzweida U, Stevens B (2020) Climate statistics in global simulations of the atmosphere, from 80 to 2.5 km grid spacing. J Meteorol Soc Jpn Ser II 98:73–91. https://doi.org/10.2151/jmsj.2020-005

Hong S-Y, Lim J-OJ (2006) The WRF single-moment 6-Class Microphysics Scheme (WSM6). J Korean Meteorol Soc 42:129–151

Hong S-Y, Noh Y, Dudhia J (2006) A new vertical diffusion package with an explicit treatment of entrainment processes. Mon Weather Rev 134:2318–2341. https://doi.org/10.1175/MWR3199.1

Huang X, Rhoades AM, Ullrich PA, Zarzycki CM (2016) An evaluation of the variable-resolution CESM for modeling California's climate. J Adv Model Earth Syst 8:345–369. https://doi.org/10.1002/2015ms000559

Huffman GJ, Stocker EF, Bolvin DT, Nelkin EJ, Tan J (2019) GPM IMERG final precipitation L3 half hourly 0.1 degree x 0.1 degree V06, Greenbelt, MD, Goddard Earth Sciences Data and Information Services Center (GES DISC). https://doi.org/10.5067/GPM/IMERG/3B-HH/06. Accessed: 17 Sept 2021

Iacono MJ, Delamere JS, Mlawer EJ, Shephard MW, Clough SA, Collins WD (2008) Radiative forcing by long-lived greenhouse gases: calculations with the AER radiative transfer models. J Geophys Res Atmos 113:D13103. https://doi.org/10.1029/2008JD009944

Kim H, Lee M-I, Cha D-H, Lim Y-K, Putman WM (2019) Improved representation of the diurnal variation of warm season precipitation by an atmospheric general circulation model at a 10 km horizontal resolution. Clim Dyn 53:6523–6542. https://doi.org/10.1007/s00382-019-04943-6

Lee Y-C, Wang Y-C (2021) Evaluating diurnal rainfall signal performance from CMIP5 to CMIP6. J Clim 34:7607–7623. https://doi.org/10.1175/JCLI-D-20-0812.1

Li J, Zhang Y (2022) Enhancing the stability of a global model by using an adaptively implicit vertical moist transport scheme. Meteorol Atmos Phys. https://doi.org/10.1007/s00703-022-00895-5

Li J, Chen H, Rong X, Su J, Xin Y, Furtado K, Milton S, Li N (2018) How well can a climate model simulate an extreme precipitation event: a case study using the transpose-AMIP experiment. J Clim 31:6543–6556. https://doi.org/10.1175/jcli-d-17-0801.1

Li P, Furtado K, Zhou T, Chen H, Li J (2021) Convection-permitting modelling improves simulated precipitation over the central and eastern tibetan Plateau. Q J R Meteorol Soc 147:341–362. https://doi.org/10.1002/qj.3921

Li X, Zhang Y, Peng X, Chu W, Lin Y, Li J (2022) Improved climate simulation by using a double-plume Convection Scheme in a global model. J Geophys Res Atmos. https://doi.org/10.1029/2021JD036069

Li X, Zhang Y, Lin Y, Peng X, Zhou B, Zhai P, Li J (2023) Impact of a revised trigger-closure of the double-plume convective parameterization on precipitation simulations over East Asia. Adv Atmos Sci. https://doi.org/10.1007/s00376-022-2225-9. (**in press**)

Liang X-Z (2004) Regional climate model simulation of summer precipitation diurnal cycle over the United States. Geophys Res Lett. https://doi.org/10.1029/2004gl021054

Liu Z, Zhang Y, Huang X, Li J, Wang D, Wang M, Huang X (2020) Development and performance optimization of a parallel computing infrastructure for an unstructured-mesh modelling framework. Geosci Model Dev Discuss. 2020:1–32. https://doi.org/10.5194/gmd-2020-158

Love BS, Matthews AJ, Lister GMS (2011) The diurnal cycle of precipitation over the Maritime Continent in a high-resolution atmospheric model. Q J R Meteorol Soc 137:934–947. https://doi.org/10.1002/qj.809

Michaelis AC, Lackmann GM (2019) Climatological changes in the extratropical transition of tropical cyclones in high-resolution global simulations. J Clim 32:8733–8753. https://doi.org/10.1175/jcli-d-19-0259.1

Mlawer EJ, Taubman SJ, Brown PD, Iacono MJ, Clough SA (1997) Radiative transfer for inhomogeneous atmospheres: RRTM, a validated correlated-k model for the longwave. J Geophys Res 102:16663–16682. https://doi.org/10.1029/97jd00237

Niu G-Y, Yang Z-L, Mitchell KE, Chen F, Ek MB, Barlage M, Kumar A, Manning K, Niyogi D, Rosero E, Tewari M, Xia Y (2011) The community Noah land surface model with multiparameterization options (Noah-MP): 1. Model description and evaluation with local-scale measurements. J Geophys Res Atmos 116. https://doi.org/10.1029/2010JD015139

Rahimi SR, Wu C, Liu X, Brown H (2019) Exploring a variable-resolution approach for simulating regional climate over the Tibetan Plateau using VR-CESM. J Geophys Res Atmos 124:4490–4513. https://doi.org/10.1029/2018JD028925

Roberts CD, Senan R, Molteni F, Boussetta S, Mayer M, Keeley SPE (2018) Climate model configurations of the ECMWF Integrated forecasting System (ECMWF-IFS cycle 43r1) for HighResMIP. Geosci Model Dev 11:3681–3712. https://doi.org/10.5194/gmd-11-3681-2018

Sato T, Miura H, Satoh M, Takayabu YN, Wang Y (2009) Diurnal cycle of precipitation in the tropics simulated in a global cloud-resolving model. J Clim 22:4809–4826. https://doi.org/10.1175/2009JCLI2890.1

Scaff L, Prein AF, Li Y, Liu C, Rasmussen R, Ikeda K (2019) Simulating the convective precipitation diurnal cycle in North America's current and future climate. Clim Dyn 55:369–382. https://doi.org/10.1007/s00382-019-04754-9

Shen Y, Zhao P, Pan Y, Yu J (2014) A high spatiotemporal gauge-satellite merged precipitation analysis over China. J Geophys Res Atmos 119:3063–3075. https://doi.org/10.1002/2013JD020686

Song F, Zhang GJ (2017) Improving trigger functions for convective parameterization schemes using GOAmazon observations. J Clim 30:8711–8726. https://doi.org/10.1175/jcli-d-17-0042.1

Tang S, Zhang M (2015) Three-dimensional constrained variational analysis: approach and application to analysis of atmospheric diabatic heating and derivative fields during an ARM SGP intensive observational period. J Geophys Res Atmos 120:7283–7299. https://doi.org/10.1002/2015JD023621

Tang S, Gleckler P, Xie S, Lee J, Ahn M-S, Covey C, Zhang C (2021) Evaluating diurnal and semi-diurnal cycle of precipitation in CMIP6 models using Satellite- and ground-based observations. J Clim. https://doi.org/10.1175/jcli-d-20-0639.1

Wang L, Zhang Y, Li J, Liu Z, Zhou Y (2019) Understanding the performance of an unstructured-mesh global shallow water model on kinetic energy spectra and nonlinear vorticity

dynamics. J Meteorol Res 33:1075–1097. https://doi.org/10.1007/s13351-019-9004-2

Wang Y, Zhang Y, Li X, Yuan W, Zhou Y (2022) Performance analysis of precipitation forecast by the baseline version of GRIST global 0.125-degree weather model configuration. Chin J Atmos Sci (**manuscript submitted**)

Watters D, Battaglia A (2019) The summertime diurnal cycle of precipitation derived from IMERG. Remote Sens 11:1781. https://doi.org/10.3390/rs11151781

Watters D, Battaglia A, Allan RP (2021) The diurnal cycle of precipitation according to multiple decades of Global Satellite Observations, three CMIP6 models, and the ECMWF reanalysis. J Clim 34:5063–5080. https://doi.org/10.1175/jcli-d-20-0966.1

Xie S, Wang YC, Lin W, Ma HY, Tang Q, Tang S, Zheng X, Golaz JC, Zhang GJ, Zhang M (2019) Improved diurnal cycle of precipitation in E3SM with a revised convective triggering function. J Adv Model Earth Syst 11:2290–2310. https://doi.org/10.1029/2019ms001702

Yanai M, Esbensen S, Chu J-H (1973) Determination of bulk properties of tropical cloud clusters from large-scale heat and moisture budgets. J Atmos Sci 30:611–627. https://doi.org/10.1175/1520-0469(1973)030<0611:Dobpot>2.0.Co;2

Yang Z-L, Niu G-Y, Mitchell KE, Chen F, Ek MB, Barlage M, Longuevergne L, Manning K, Niyogi D, Tewari M, Xia Y (2011) The community Noah land surface model with multiparameterization options (Noah-MP): 2. Evaluation over global river basins. J Geophys Res Atmos. https://doi.org/10.1029/2010JD015140

Yashiro H, Kajikawa Y, Miyamoto Y, Yamaura T, Yoshida R, Tomita H (2016) Resolution dependence of the diurnal cycle of precipitation simulated by a global cloud-system resolving model. Sola 12:272–276. https://doi.org/10.2151/sola.2016-053

Yu R, Li J, Chen H, Yuan W (2014) Progress in studies of the precipitation diurnal variation over contiguous China. J Meteorol Res 28:877–902. https://doi.org/10.1007/s13351-014-3272-7

Yuan W (2013) Diurnal cycles of precipitation over subtropical China in IPCC AR5 AMIP simulations. Adv Atmos Sci 30:1679–1694. https://doi.org/10.1007/s00376-013-2250-9

Yun Y, Liu C, Luo Y, Liang X, Huang L, Chen F, Rasmmusen R (2020) Convection-permitting regional climate simulation of warm-season precipitation over Eastern China. Clim Dyn 54:1469–1489. https://doi.org/10.1007/s00382-019-05070-y

Zarzycki CM, Jablonowski C (2014) A multidecadal simulation of Atlantic tropical cyclones using a variable-resolution global atmospheric general circulation model. J Adv Model Earth Syst 6:805–828. https://doi.org/10.1002/2014ms000352

Zhang Y (2018) Extending high-order flux operators on spherical icosahedral grids and their applications in the framework of a shallow water model. J Adv Model Earth Syst 10:145–164. https://doi.org/10.1002/2017ms001088

Zhang Y, Chen H (2016) Comparing CAM5 and superparameterized CAM5 simulations of summer precipitation characteristics over Continental East Asia: mean state, frequency–intensity relationship, diurnal cycle, and influencing factors. J Clim 29:1067–1089. https://doi.org/10.1175/jcli-d-15-0342.1

Zhang C, Wang Y (2017) Projected future changes of tropical cyclone activity over the Western North and South Pacific in a 20-km-mesh regional climate model. J Clim 30:5923–5941. https://doi.org/10.1175/jcli-d-16-0597.1

Zhang Y, Chen H, Wang D (2019a) Robust nocturnal and early morning summer rainfall peaks over Continental East Asia in a global multiscale modeling framework. Atmosphere. https://doi.org/10.3390/atmos10020053

Zhang Y, Li J, Yu R, Zhang S, Liu Z, Huang J, Zhou Y (2019b) A layer-averaged nonhydrostatic dynamical framework on an unstructured mesh for global and regional atmospheric modeling: model description, baseline evaluation, and sensitivity exploration. J Adv Model Earth Syst 11:1685–1714. https://doi.org/10.1029/2018ms001539

Zhang Y, Li J, Yu R, Liu Z, Zhou Y, Li X, Huang X (2020) A multiscale dynamical model in a dry-mass coordinate for weather and climate modeling: moist dynamics and its coupling to physics. Mon Weather Rev 148:2671–2699. https://doi.org/10.1175/mwr-d-19-0305.1

Zhang Y, Yu R, Li J, Li X, Rong X, Peng X, Zhou Y (2021) AMIP Simulations of a global model for Unified Weather-Climate Forecast: understanding precipitation characteristics and sensitivity over East Asia. J Adv Model Earth Syst 13:e2021MS002592. https://doi.org/10.1029/2021MS002592

Zhang Y, Li X, Liu Z, Rong X, Li J, Zhou Y, Chen S (2022) Resolution sensitivity of the GRIST nonhydrostatic model from 120 to 5 km (3.75 km) during the DYAMOND winter. Earth Space Sci. https://doi.org/10.1029/2022ea002401

Zhao C, Xu M, Wang Y, Zhang M, Guo J, Hu Z, Leung LR, Duda M, Skamarock W (2019) Modeling extreme precipitation over East China with a global variable-resolution modeling framework (MPASv5.2): impacts of resolution and physics. Geosci Model Dev 12:2707–2726. https://doi.org/10.5194/gmd-12-2707-2019

Zhou Y, Zhang Y, Li J, Yu R, Liu Z (2020) Configuration and evaluation of a global unstructured mesh atmospheric model (GRIST-A20.9) based on the variable-resolution approach. Geosci Model Dev 13:6325–6348. https://doi.org/10.5194/gmd-13-6325-2020